Sensors & Diagnostics

PAPER

View Article Online
View Journal | View Issue

Cite this: *Sens. Diagn.*, 2024, **3**, 872

Detection of TNP and sulfite ions in an aqueous medium using a pyrazinium-based chemosensor†

Pragya,[a] Krishnan Rangan [b] and Bharti Khungar *[a]

Received 4th January 2024,
Accepted 13th April 2024

DOI: 10.1039/d3sd00345k

rsc.li/sensors

A fluorescent pyrazinium-based 1-benzyl-3,5-diphenylpyrazin-1-ium bromide (**BPPyz**) chemosensor was synthesized and well-characterized. A significant reduction in blue emission of **BPPyz** was observed in the presence of TNP as compared to other nitroaromatic compounds, indicating high selectivity towards TNP. In the presence of sulfite ions, **BPPyz** showed fluorescence quenching and rapid naked-eye detection with a significant color change. The sensing mechanism was investigated through UV–visible studies, time-resolved fluorescence results, and density functional theory (DFT) calculations. The quenching constants (K_{SV}) are 4.12×10^5 M^{-1} for TNP and 3.8×10^5 M^{-1} for sulfite with the detection limits of 9.5 nM and 46.17 nM for TNP and sulfite, respectively. The selectivity of **BPPyz** towards TNP was ascribed to the ground state charge transfer complex (GSC) formation and resonance energy transfer. Sulfite ion detection involved the formation of a GSC through hydrogen bonding with the pyrazinium proton.

1. Introduction

Detection of high-energy nitroexplosive is required due to environmental pollution and homeland security.[1] Aromatic nitro compounds, such as 1,3,5-trinitroperhydro-1,3,5-triazine (RDX), 2,4-dinitrotoluene (2,4-DNT), and 2,4,6-trinitrotoluene (TNT), are commonly used as explosives.[2] 2,4,6-trinitrophenol acid (TNP) is more lethal than TNT due to its fast detonation velocity and low safety coefficient.[3] It is extensively utilized in leather, dye, pharmaceutical,[4] and fireworks industries and rocket fuel production.[5] Because of its diverse uses, high water solubility, and low degradation, it can easily contaminate water and soil[6] and is therefore recognized as an environmental pollutant.[7] TNP carries health risks, including cancer, skin irritation, liver dysfunction, respiratory organ damage, nausea, and allergies.[8,9] The allowed concentration of TNP in groundwater is 0.001 mg L^{-1} according to the WHO. To monitor environmental contamination and terrorist operations, selective and sensitive detection of TNP is needed.[10]

Sulfite is used as an antioxidant, antibacterial, and enzyme inhibitor in food and beverages.[11] Ingress of sulfite into the human body is through SO_2, an environmental pollutant released by unrestricted combustion of fossil fuels and volcanic activity.[12] In an aqueous solution at neutral pH, SO_2 exists in equilibrium between sulfite ions (SO_3^{2-}) and bisulfite ions (HSO_3^-). An abnormal level of exogenous sulfite in humans induces a free radical reaction, changing the oxidation and antioxidant levels and causing symptoms such as allergies, asthma, diarrhea, and hypotension.[13] Abnormal endogenous sulfite has been linked to neurological diseases and lung cancer.[14] The WHO considers a daily sulfite intake of less than 0.7 mg kg^{-1}.[15] Therefore, detecting sulfite with selectivity and sensitivity in the environment is essential.

Various instrumental techniques are employed to detect TNP, such as gas chromatography–mass spectrometry (GC-MS),[16] high-performance liquid chromatography (HPLC),[17] surface-enhanced Raman spectroscopy,[18] and ion-mobility spectroscopy.[19] A diverse range of molecules based on naphthalimide,[20] pyrene,[21] triazine,[22] benzimidazole,[23] rhodamine,[24] and bisthiocarbonohydrazone[25] are reported for the detection of TNP. The detection mechanism involves photo-induced electron transfer (PET),[26] ground state charge transfer complex (GSC) formation,[27] resonance energy transfer (RET),[28] intramolecular charge transfer (ICT),[29] the inner filter effect (IFE),[30] and indicator displacement assay (IDA).[31]

The conventional methods to detect sulfite include the official Monier-Williams methods,[32] titrimetry,[33] electrochemical methods, chromatography,[34] flow injection analysis, and capillary electrophoresis.[35] Pyrazoline,[36] BODIPY,[37] coumarin,[38] and fluorescein[39]-based molecules are designed to detect SO_3^{2-}. The mechanism involved in sulfite ion detection includes hydrogen bond-inhibited C=N isomerization,[40] hydrogen bonding recognition,[41]

[a] *Department of Chemistry, Birla Institute of Technology and Science Pilani, Pilani Campus, Pilani, Rajasthan, 333031, India.*
E-mail: bkhungar@pilani.bits-pilani.ac.in
[b] *Department of Chemistry, Birla Institute of Technology and Science Pilani, Hyderabad Campus, Secunderabad, Telangana, 500078, India*

† Electronic supplementary information (ESI) available. CCDC 2189176 and 2189177. For ESI and crystallographic data in CIF or other electronic format see DOI: https://doi.org/10.1039/d3sd00345k

deprotection of the levulinate group,[42] the Michael addition reaction,[43] and nucleophilic reaction.

Fluorescence-based detection has gained tremendous attention because of its high sensitivity, ease of use, and rapid execution time.[44,45] Several fluorescent chemosensors reported in the literature for TNP and sulfite detection are associated with drawbacks such as lower water solubility, analyte interference, and low detection limits. Therefore, it is necessary to develop fluorescent chemosensors with multianalyte sensing, a low detection limit, and high water solubility for TNP and SO_3^{2-}. Ion-tagged compounds are a fascinating class of organic materials because of their distinctive, tunable characteristics that result from possible combinations of cations and anions.[46,47] Pyrazine derivatives exhibit excellent photostability and are often employed as luminescent materials.[48] Moreover, quaternization of one of the N atoms of the pyrazine core can enhance the hydrophilicity of the molecules, thereby enabling the applications in an aqueous medium. In continuation to our work on pyrazinium-based chemosensors,[49] herein we report the synthesis of another pyrazinium-based chemosensor, **BPPyz**, and its use as a fluorescence sensing probe for TNP and colorimetric and fluorimetric detection of sulfite ions at room temperature in an aqueous medium.

2. Experimental section

2.1 Materials and instruments

The reagents were utilized without additional purification after being purchased from commercial suppliers. Milli-Q water was used to prepare stock solutions for various experiments. ^{1}H NMR (400 MHz) and $^{13}C\{^1H\}$ NMR (100 MHz) spectra were recorded using TMS as an internal standard and $CDCl_3$ or DMSO-d_6 as solvents. Parts per million (ppm) and hertz (Hz) are used to express chemical shifts (δ) and coupling constants (J), respectively. In the ^{1}H NMR spectra, spin multiplicities are represented by the following abbreviations: s = singlet, d = doublet, t = triplet, and m = multiplet. An Agilent 6545 Q-TOF LC/MS spectrometer with an ESI source in both the positive and negative modes was used to analyze the mass spectra of the synthesized compounds. Melting points were measured in open glass capillaries using MPA120 automated melting point apparatus and were uncorrected. Absorption studies were conducted on a JASCO V-650 spectrophotometer using 10 mm path length quartz cuvettes in the wavelength range of 200–700 nm, and fluorescence measurements were performed on a Horiba Fluoromax-4 spectrofluorometer using 10 mm path length quartz cuvettes with a slit width of 3 nm. Fluorescence lifetime measurements were carried out using an Edinburgh FL920 fluorescence lifetime spectrometer. The sample was excited using a laser diode at 370 nm. All spectroscopic measurements were performed at room temperature. Data collection and reduction for single-crystal XRD were carried out utilizing CrysAlis PRO on a single-crystal Rigaku Oxford XtaLab Pro Kappa dual home/near diffractometer. The crystal was kept at 293(2) K during data collection using a CuKα (λ = 1.54184 Å) radiation source. Using Olex2,[50] the structure was solved with the ShelXT[51] structure solution program using Intrinsic Phasing and refined with the ShelXT[52] refinement package using Least Squares minimization. The optimized structures and HOMO–LUMO states of the molecules were obtained by density functional theory (DFT)-based quantum chemical calculations at the level of B3LYP (Becke three-parameter exchange functional and Lee–Yang–Parr correlation functional)[53] and standard 6-311G (d,p)[54] in the Gaussian09 program suite.[55] For the colorimetric read-out using a smartphone, a paper box with a black plastic board covering it on the outside was utilized. To provide even lighting, 3.0 W lamps were mounted on either side of the upper surface. The smartphone was placed five centimeters away from the sample holder containing an aqueous solution of **BPPyz** with various concentrations of SO_3^{2-}. The smartphone built-in camera was used to take pictures with the best resolution available. To extract the RGB values from the photos, the colorgrab app was utilized.

2.2 Synthesis of 2,6-diphenylpyrazine (PPyz)

A round-bottom flask was charged with 2,6-dichloropyrazine (0.671 mmol), phenylboronic acid (1.476 mmol), $Pd(OAc)_2$ (0.033 mmol), and K_2CO_3 (1.342 mmol) in dimethylformamide (2.5 mL). The reaction mixture was irradiated in a microwave at 120 °C for 50 min. The reaction mixture was cooled to room temperature, quenched with water (5 mL), and diluted with EtOAc (15 mL). The layers were separated, and the aqueous layer was extracted three times with 10 mL of EtOAc. The organic layer was dried over Na_2SO_4, filtered, and concentrated under reduced pressure. The residue was purified by column chromatography on a silica gel using a 15–20% EtOAc/hexane mixture. **PPyz** was obtained as a white solid (137 mg, 86% yield); mp = 98–100 °C; δ ^{1}H NMR (400 MHz, $CDCl_3$) δ 9.00 (s, 2H), 8.21–8.17 (m, 4H), 7.60–7.50 (m, 6H). $^{13}C\{^1H\}$ NMR (100 MHz, $CDCl_3$) δ 151.6, 139.9, 136.5, 129.9, 129.0, 127.0; HRMS (ESI) m/z: $[M + H]^+$ calcd for $[C_{16}H_{12}N_2 + H]^+$, 233.1002, found 233.1002.

2.3 Synthesis of 1-benzyl-3,5-diphenyl pyrazin-1-ium bromide (BPPyz)

A mixture of **PPyz** (0.431 mmol) and benzyl bromide (0.517 mmol) was stirred in a round-bottom flask for 8 h at 75 °C. The reaction mixture was washed with ethyl acetate, and the bright yellow solid obtained was filtered and dried under vacuum (169 mg, 97.1% yield); mp = 201–210 °C; ^{1}H NMR (400 MHz, DMSO-d_6) δ 9.77 (s, 2H), 8.37–8.29 (m, 4H), 7.73 (dd, J = 8.0, 2.4 Hz, 2H), 7.68 (dd, J = 5.2, 2.0 Hz, 6H), 7.49–7.44 (m, 3H), 5.95 (s, 2H). $^{13}C\{^1H\}$ NMR (100 MHz, DMSO-d_6) δ 153.1, 138.4, 134.4, 133.1, 131.2, 130.2, 130.1, 130.0, 129.6, 129.5, 65.2; HRMS (ESI) m/z: $[M - Br]^+$ calcd for $[C_{23}H_{19}N_2]^+$, 323.1543; found 323.1536.

2.4 Synthesis of the BPPyz–TNP complex

At room temperature, an ethanolic solution of TNP (0.247 mmol) was added dropwise to a solution of **BPPyz** (0.247 mmol) in ethanol. The reaction mixture was stirred for 5 h, and the obtained yellow precipitated solid was filtered and washed with ethyl acetate (130 mg, 95%); mp = 220–225 °C; ^{1}H NMR (400 MHz, DMSO-d_6) δ 9.75 (s, 2H), 8.56 (s, 2H), 8.32 (dd, J = 6.8, 2.8 Hz, 4H), 7.73–7.70 (m, 2H), 7.67 (dd, J = 5.2, 2.0 Hz, 5H), 7.46 (dd, J = 5.2, 1.8 Hz, 3H), 5.94 (s, 2H); HRMS (ESI) m/z: $[M - Br]^+$ calcd for $[C_{23}H_{19}N_2]^+$, 323.1543; found 323.1536.

2.5 Synthesis of the BPPyz–SO_3^{2-} complex

An acetonitrile solution of **BPPyz** (0.247 mmol) was added dropwise to a solution of sodium sulfite (0.123 mmol) at room temperature. The reaction mixture was stirred for 5 min, and the yellow precipitated solid was filtered and washed with ethyl acetate, (125 mg, 70%); mp = 215–225 °C ^{1}H NMR (400 MHz, DMSO-d_6) δ 10.01 (s, 2H), 8.39 (dd, J = 6.6, 3.0 Hz, 4H), 7.86–7.82 (m, 2H), 7.68 (dd, J = 4.8, 1.6 Hz, 6H), 7.46 (dq, J = 3.7, 1.9 Hz, 2H), 6.05 (s, 2H). ^{13}C{^{1}H} NMR (100 MHz, DMSO-d_6) δ 157.3, 133.7, 133.6, 132.9, 132.5, 130.1, 130.0, 129.7, 129.6, 128.1, 65.1; HRMS (ESI) m/z: $[M - Br]^+$ calcd for $[C_{23}H_{19}N_2]^+$, 323.1543; found 323.1538.

3. Results and discussion

3.1 Synthesis and characterization

BPPyz was synthesized by the Suzuki coupling reaction of 2,6-dichloropyrazine with phenylboronic acid to give 2,6-diphenylpyrazine (**PPyz**) (Fig. S1–S3†) followed by a solvent-free reaction between **PPyz** and benzyl bromide (Scheme 1). **BPPyz** was characterized using different spectroscopic techniques and single-crystal XRD. In the ^{1}H NMR spectrum of **BPPyz**, a two-proton singlet at 5.65 ppm indicated the presence of benzylic protons, and aromatic protons appeared in the range of 7.09–8.26 ppm (Fig. S4†). In the ^{13}C NMR spectrum of **BPPyz**, a signal at 65.1 ppm was due to the benzylic carbon, and the aromatic carbon signals appeared in the 128.1–157.4 ppm range (Fig. S5†). ESI mass spectral analysis showed an m/z peak at 323.1536, which may be attributed to [**BPPyz**–Br]$^+$ (Fig. S6†). The structure of **BPPyz** was further confirmed by single-crystal XRD analysis (CCDC number 2189176). The compound crystallized in the monoclinic $P2_1/c$ space group. The ionic compound comprises an organic cation and a bromide anion; three pairs of these ions are found in the crystallographic asymmetric unit, Z' = 3. The ORTEP diagram shown is only for one molecule in Fig. 1 (Fig. S7†).

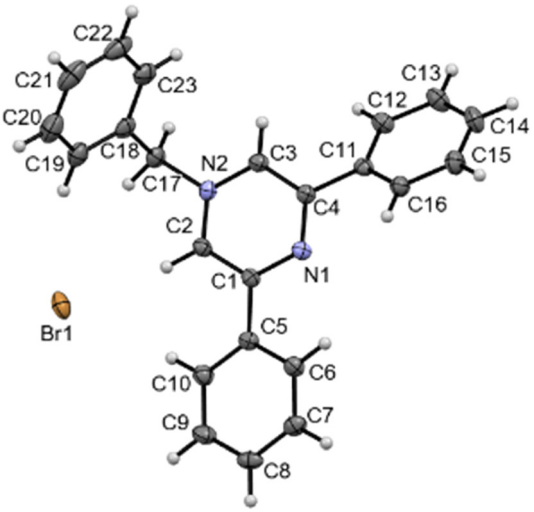

Fig. 1 ORTEP diagram of **BPPyz**. CCDC 2189176.

3.2 Response of BPPyz toward TNP

Nitroaromatic compounds (NACs) can interact with fluorescent probes through non-covalent and electrostatic interactions resulting in a change in the absorption and emission properties. **BPPyz** showed three absorption bands at λ_{max} = 356 nm, 268 nm, and 236 nm in an aqueous medium. It also showed a strong emission (Φ = 0.35) maximum at 438 nm (λ_{ex} = 359 nm) in the fluorescence spectra (Fig. S8†). The blue emission of **BPPyz** in an aqueous medium motivated us to explore its potential application as a fluorescent chemosensor (Fig. S9†). The UV–visible spectrum of **BPPyz** was examined by adding nitroaromatics 4-NT, 4-NP, NM, 4-NBA, NB, 3,4-DNT, and 2,4-DNP in 2 × 10^{-5} M concentration. No alteration was observed in the absorbance intensity with these NACs except for TNP, which showed an increase in the intensity with the appearance of a new band at 425 nm (Fig. S10†). The fluorescence intensity of **BPPyz** on the addition of 2,4-DNP, 4-NP, and TNP showed fluorescence quenching, whereas other NACs showed insignificant

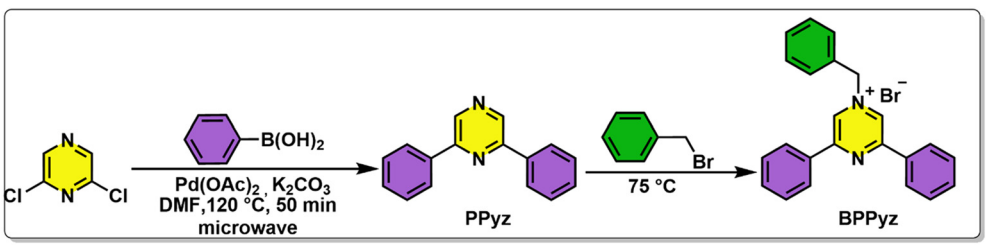

Scheme 1 Synthesis of 1-benzyl-3,5-diphenylpyrazin-1-ium bromide (**BPPyz**).

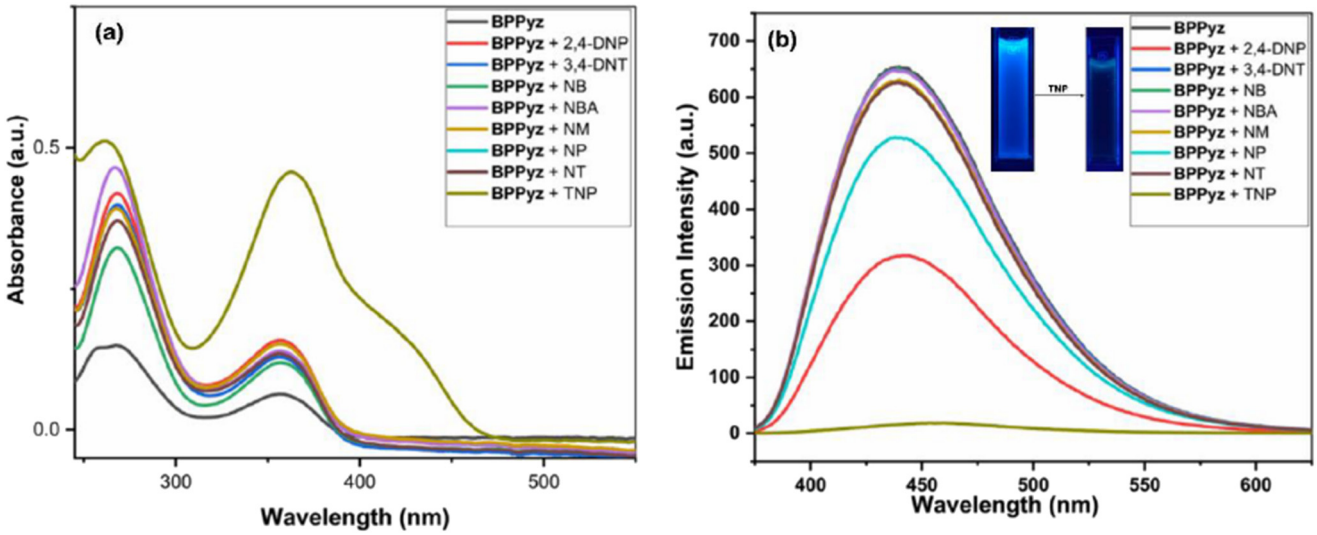

Fig. 2 (a) Absorbance and (b) fluorescence spectra of **BPPyz** (2×10^{-5} M) with different nitroaromatic analytes.

changes (Fig. 2). The quenching efficiencies of TNP, 2,4-DNP, and 4-NP were found to be 97.3%, 75%, and 40%, respectively (Fig. S11†).

So far, the selectivity of **BPPyz** towards TNP was established among different nitro compounds. Further, interference studies were performed using competitive binding studies for TNP with **BPPyz** in the presence of equimolar concentrations (2×10^{-5} M) of other metal ions (Na^+, Mg^{2+}, Al^{3+}, K^+, Ca^{2+}, Mn^{2+}, Fe^{2+}, Fe^{3+}, Co^{2+}, Ni^{2+}, Cu^{2+}, Zn^{2+}, Ag^+, Cd^{2+}, Hg^{2+}, Pb^{2+}, La^{3+}, Eu^{3+}, Gd^{3+} and Yb^{3+}), anions (CH_3COO^-, HCO_3^-, NO_3^-, I^-, Br^-, Cl^-, and F^-) and nitro compounds (4-NT, 4-NP, NM, 4-NBA, NB, 3,4-DNT, and 2,4-DNP) (Fig. S12†). No perturbation of fluorescence quenching was observed, which established the selectivity of **BPPyz** for TNP in the presence of several other analytes. The behavior of **BPPyz** towards TNP in different pH solutions was also investigated. On the addition of TNP, the maximum fluorescence quenching of **BPPyz** was found to be in the pH range of 6–8. This result indicated that **BPPyz** can be used efficiently as a fluorescent chemosensor for TNP detection under a neutral pH environment (Fig. S13†).

The general mechanisms of fluorescence quenching include static and/or dynamic quenching, Förster resonance energy transfer (FRET), photo-induced electron transfer (PET), and the inner filter effect (IFE). Absorbance and fluorescence titrations were performed to elucidate the mechanism of interactions between **BPPyz** and TNP. On the continuous addition of TNP, the absorption intensity of the band at 358 nm increased, and a new band at 425 nm appeared due to the formation of a ground state charge transfer complex. The intensity of the emission peak at 438 nm decreased with a gradual increase in the TNP

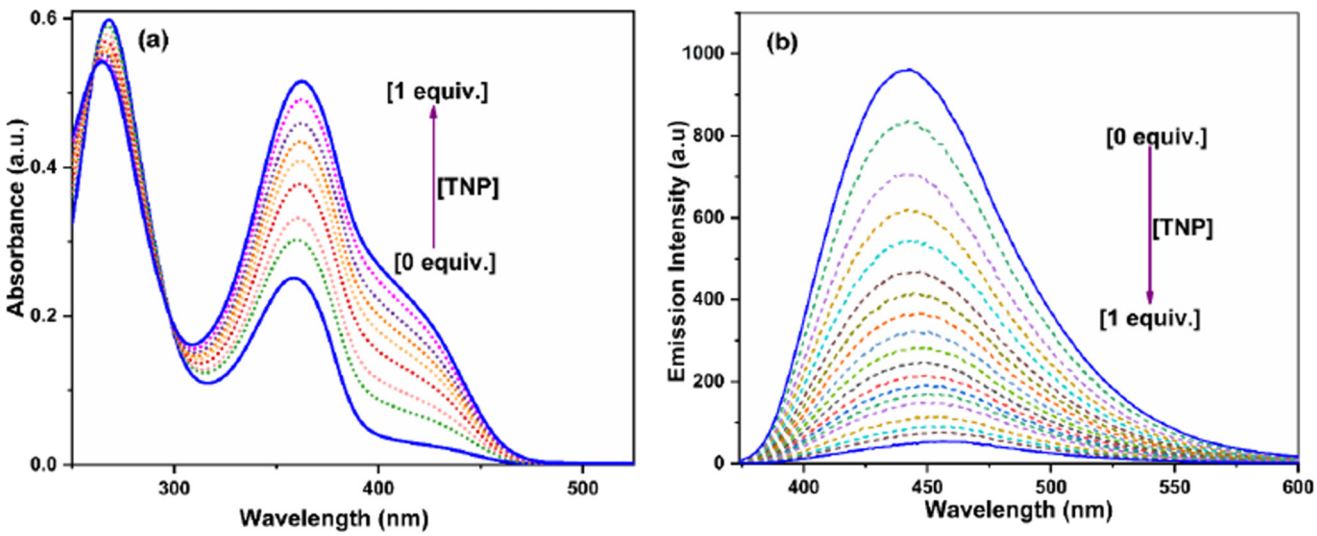

Fig. 3 (a) Absorbance and (b) fluorescence spectra of **BPPyz** (2×10^{-5} M) with different amounts of TNP.

concentration (Fig. 3). This is due to the formation of the picrate anion by the deprotonation of the phenolic –OH of TNP in an aqueous medium, followed by an anion exchange with Br^-.[56] Fluorescence titration studies were also performed for 2,4-DNP and 4-NP to investigate the quenching of **BPPyz** (Fig. S14 and S15†). The emission intensity at 438 nm decreased in the presence of 2,4-DNP and 4-NP, but to a lesser extent than TNP.

The detection limit (DL) obtained from fluorescence titration studies at 438 nm was found to be 9.5 nM. The limit of detection (LOD) value was estimated by the IUPAC standard method, LOD = $y_{blank} + 3 \times SD_{blank}$, where y_{blank} is the average signal intensity at zero and SD_{blank} is the standard deviation of the blank measurements (Fig. S16†).[57,58]

To examine the sensitivity of **BPPyz** toward TNP, the Stern–Volmer (S–V) constant (K_{SV}) was calculated using the Stern–Volmer equation, $I_0/I = 1 + K_{SV}[Q]$, where I_0 represents the initial fluorescence intensity in the absence of the analyte, I denotes the intensity in the presence of the analyte, [Q] is the molar concentration of the analyte and K_{SV} is the quenching constant. The quenching constant (K_{SV}) for **BPPyz** was found to be 4.12×10^5 M^{-1}, confirming the high sensitivity of **BPPyz** toward TNP (Fig. S17†). The K_{SV} values were also calculated for 2,4-DNP and 4-NP and were found to be 6.7×10^3 M^{-1} and 2.3×10^4 M^{-1}, respectively (Fig. S18 and S19†). A Stern–Volmer plot may be linear or nonlinear depending on the static or dynamic quenching process. The linear S–V plot at the lower concentration indicated static quenching, which was attributed to the formation of the ground state charge transfer complex. This was confirmed by the appearance of a new band at 425 nm in the UV–visible spectra. The correlation coefficient (R^2), obtained *via* regression analysis, was computed to be 0.998.

The deviation from linearity of the S–V plot at higher concentrations revealed the possibility of dynamic quenching. Dynamic quenching occurs as a result of collisional interactions or excited-state phenomena like Förster resonance energy transfer (FRET). Energy transfer through FRET is dependent on (i) a significant overlap between the absorbance and fluorescence spectra of the acceptor and donor, respectively, (ii) relative dipole orientations of the donor and acceptor, and (iii) the Förster distance between the donor and acceptor.

To validate the dynamic quenching mechanism, UV–visible absorption spectra of TNP were plotted together with the emission spectrum of **BPPyz**, and an effective overlap was observed with TNP only. Therefore, resonance energy can easily be transferred from the excited donor fluorophore (**BPPyz**) to the electron-deficient acceptor (TNP).[59] To identify the extent of energy transfer, the overlap integral value (J_λ) for TNP was calculated and found to be 5.74×10^{14} M^{-1} cm^{-1} nm^{-4}. The Förster distance, R_0 for the **BPPyz**–TNP interaction, was 38.10 Å, which falls in the range for RET (Fig. S20†). The spectral overlap of the absorption spectra of the absorber with the emission/excitation spectra of the fluorophore also indicates the possibility of an inner filter effect. The species in the IFE process should not chemically interact with each other, *i.e.*, no new absorption band of the ground state charge transfer complex should be observed. Further, the quencher should not change the fluorescence lifetime of the fluorophore. In the current study, a new absorption band at 425 nm was observed due to the ground state charge transfer complex formation. Furthermore, fluorescence lifetime decay profiles also showed a decrease in the lifetime of the **BPPyz**–TNP complex (0.5 ns) compared to **BPPyz** (3.50 ns). Moreover, it was observed that the reduction in the fluorescence lifetime and intensity followed the relation $\tau_0/\tau = I_0/I$, which is a crucial feature of collisional or dynamic quenching (Fig. S21†).

Further, to exclude the possibility of the IFE, corrections were performed using eqn (1):

$$I_{corr}/I_{obs} = 10^{(A_{ex}+A_{em})/2} \quad (1)$$

where I_{corr} and I_{obs} indicate the fluorescence intensities of **BPPyz** after and before IFE corrections, respectively. A_{ex} and A_{em} denote the absorbances of the sensing system at the excitation and emission of **BPPyz**, respectively. No change in the emission intensity after performing IFE corrections clearly indicated the non-involvement of the IFE in the TNP sensing mechanism (Fig. S22†).

The emission of **BPPyz** was recorded in the presence of triflic acid (TFA) ($pK_a \sim 0.52$), a stronger acid than TNP ($pK_a \sim 0.38$), to investigate the acidity effect of TNP on fluorescence quenching. No change in the fluorescence emission suggested that the acidity effect was not involved in the fluorescence quenching mechanism (Fig. S23†).

The nature of the attenuation of the fluorescence emission of **BPPyz** by TNP was inspected by ^1H NMR, HRMS, and theoretical studies. The stoichiometric ratio was confirmed by the spectroscopic analysis of the yellow complex isolated from the ethanolic solution of **BPPyz** and TNP at room temperature. Comparing the ^1H NMR spectra of **BPPyz** and the **BPPyz**–TNP complex suggested the complexation of the picrate ion with the **BPPyz** cation (Fig. 4). In the ^1H NMR spectrum of the **BPPyz**–picrate complex, a new prominent signal at 8.58 ppm due to picrate protons and their relative integration confirmed the formation of a 1 : 1 molar complex between **BPPyz** and TNP (Fig. S24†).

The HRMS analysis of **BPPyz**–TNP demonstrated m/z peaks attributed to the anionic $[TNP–H]^-$ and cationic $[BPPyz–Br]^+$ species at 227.9525 and 323.1536, respectively (Fig. S25†). The crystal of **BPPyz**–TNP grown from an acetonitrile–methanol solvent mixture crystallized in the monoclinic system ($C2/c$ space group). One $\mathbf{BPPyz}^+$ cation and one deprotonated picrate anion are found in the crystallographic asymmetric unit, $Z' = 1$. The ORTEP diagram of the **BPPyz**–TNP crystal is shown in Fig. 5. The **BPPyz**–TNP complex is stabilized through short C–H···O non-covalent interactions. The pyrazine ring C3–H3···O1, methylene C17–H17A···O1, and phenyl ring C3–H3···O1 non-covalent bond distances are 2.391, 2.471, and 2.533 Å, respectively; these bond distances are shorter than the hydrogen–oxygen van der Waals radius, 2.72 Å.

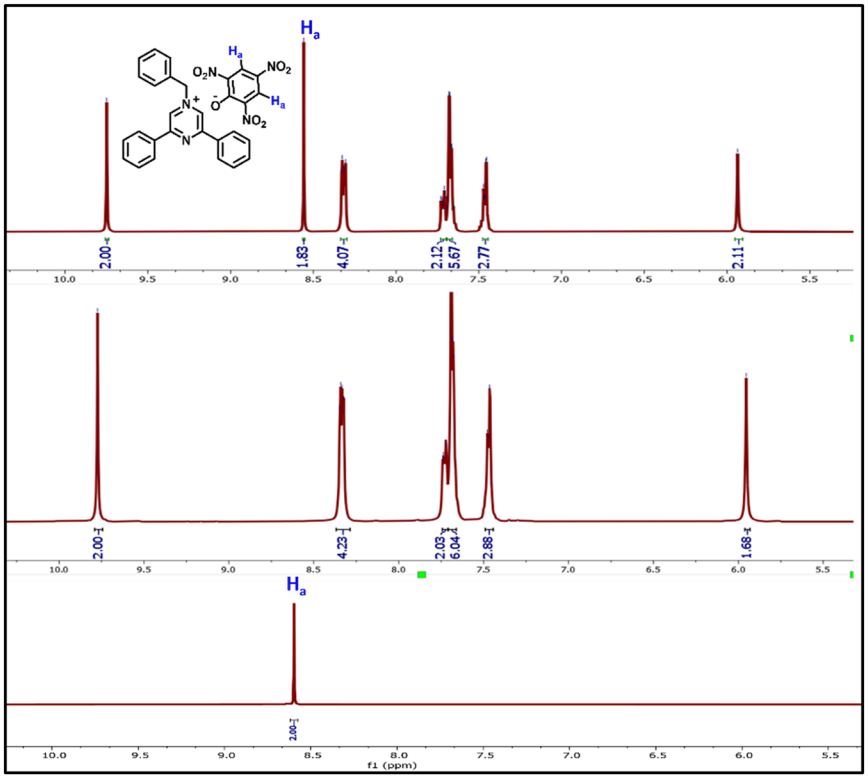

Fig. 4 ^{1}H NMR spectra of the **BPPyz**–TNP complex.

To study the interaction between **BPPyz** and TNP, DFT calculations were performed at the level of B3LYP/ 6-311G(d,p) in the gas phase. The energies of the highest occupied molecular orbital (HOMO) and the lowest occupied molecular orbital (LUMO) of **BPPyz** were −9.856 eV and −6.334 eV, respectively. The energies of the HOMO and LUMO of the picrate anion were found to be −3.424 eV and +0.1417 eV, respectively (Fig. 6). Hence, theoretical results direct the possibility of a ground state electronic charge transfer from the HOMO of the picrate anion to the LUMO of **BPPyz**, which results in high quenching efficiency. However, the HOMOs of other nitroaromatics were found to have lower energy levels

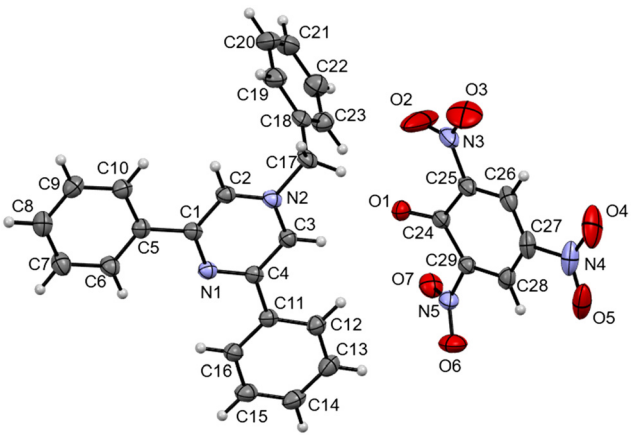

Fig. 5 ORTEP diagram of **BPPyz**–TNP (CCDC 2189177).

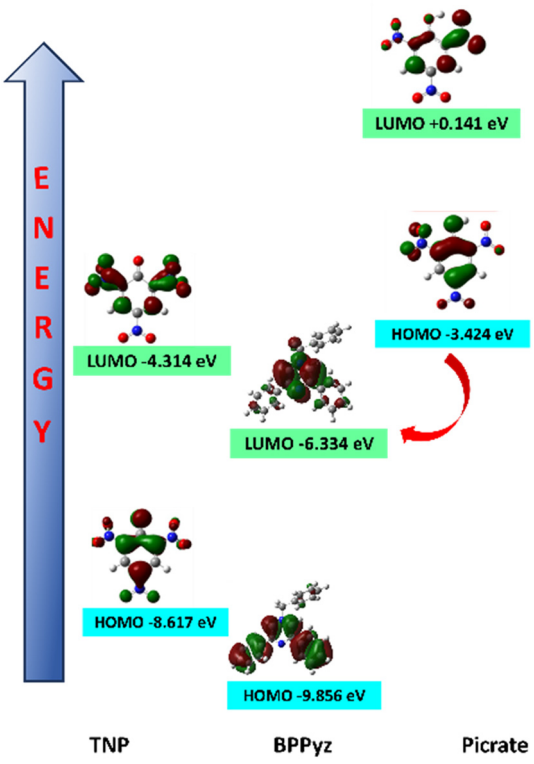

Fig. 6 Energy levels and profiles of the frontier molecular orbitals of **BPPyz**, picrate, and TNP.

than the LUMO of **BPPyz**, thereby discarding the possibility of electronic charge transfer and leading to low quenching efficiencies (Fig. S26†).

3.3 Response of BPPyz toward SO_3^{2-}

The anion sensing ability of the probe **BPPyz** was elucidated by the changes in the UV–visible and fluorescence spectra upon the addition of various anions, SO_3^{2-}, HSO_3^-, NO_3^-, F^-, Cl^-, Br^-, I^-, ClO_4^-, $[Fe(CN)_5(NO)]^{2-}$, $C_2O_4^{2-}$, cystine, glutathione, methionine, $S_2O_3^{2-}$, SO_4^{2-}, PO_4^{2-}, CN^-, SCN^-, N_3^-, OH^-, $H_2PO_4^-$, and OAc^- (2×10^{-5} M) in aqueous media. Among these anions, **BPPyz** was interestingly selective to SO_3^{2-} with a visual change in the color of the solution from colorless to yellow. On the addition of SO_3^{2-} ions, the UV–visible absorption bands of **BPPyz** at 268 nm and 358 nm showed a hypsochromic shift to 255 nm and 322 nm, respectively, with a simultaneous emergence of a new band at 439 nm. The **BPPyz** solution emitted dark brownish fluorescence in the presence of the SO_3^{2-} anion under a 365 nm UV lamp. To ascertain the selectivity of the probe, emission spectra of **BPPyz** were recorded in the presence of various anions at 2×10^{-5} M concentration, and no alteration was observed in the emission behavior of **BPPyz**. The addition of SO_3^{2-} resulted in 94.3% quenching of the emission intensity at 438 nm. A ground state charge transfer complex might have formed due to the exchange of Br^- with SO_3^{2-} (Fig. 7).

To further confirm the formation of the ground state charge transfer complex, UV–vis titration studies of **BPPyz** were performed with the increasing concentration of SO_3^{2-}. A well-defined isosbestic point at 385 nm suggested the formation of a new compound upon treatment of the probe with sulfite ions. To better understand the sensing ability of **BPPyz** for the SO_3^{2-} anion, a fluorescence titration experiment of **BPPyz** was carried out with the gradual addition of SO_3^{2-}. The fluorescence intensity of **BPPyz** decreased gradually with the increasing concentration of the SO_3^{2-} anion (Fig. 8). The linear variation at low concentration was due to static quenching. The linear fit of the plot provided $K_{SV} = 3.8 \times 10^5$ M^{-1} and a correlation coefficient (R^2) of 0.9936 (Fig. S27†). The deviation from linearity indicated dynamic quenching, which was further supported by lifetime measurements. Fluorescence lifetime decay profiles showed a decrease in the lifetime of the **BPPyz**-SO_3^{2-} complex (0.9 ns) as compared to **BPPyz** (3.50 ns) due to dynamic quenching (Fig. S21†). The Job plot suggested a 2 : 1 stoichiometry between **BPPyz** and the SO_3^{2-} anion (Fig. S28†).

The selectivity of **BPPyz** for SO_3^{2-} was evaluated by monitoring the fluorescence response of **BPPyz** toward SO_3^{2-} in the presence of F^-, Cl^-, Br^-, I^-, NO_3^-, HCO_3^-, CH_3COO^-, $S_2O_3^{2-}$, SO_4^{2-}, and PO_4^{2-} (Fig. S29†). Fluorescence quenching was unaffected, indicating that **BPPyz** can selectively discriminate the SO_3^{2-} anion in the presence of all other examined anions. The detection limit is also an important parameter that describes the sensing ability of sensors. The detection limit of **BPPyz** for the SO_3^{2-} anion was found to be 46.17 nM (Fig. S30†). The maximum fluorescence quenching of **BPPyz** in the presence of SO_3^{2-} was found in the pH range of 6–9, indicating its stability in a neutral pH environment (Fig. S13†).

To further confirm the stoichiometric ratio of the complex, the dark yellow complex was isolated from an ethanolic solution of **BPPyz** and SO_3^{2-} at room temperature and was analyzed by ^1H and ^{13}C NMR (Fig. S31 and 32†). In the HRMS spectrum of the **BPPyz**–SO_3^{2-} complex, the *m*/*z* peak was observed at 323.1536 for $[\mathbf{BPPyz}–Br]^+$ (Fig. S33†). In the ^1H NMR spectrum of the **BPPyz**–SO_3^{2-} complex, the pyrazinium proton H_a shifted downfield from 9.77 ppm to 10.01 ppm. The prominent shift in the ^1H NMR spectrum indicated the hydrogen bonding between the pyrazinium proton (H_a) of **BPPyz** and the O atom of SO_3^{2-}. A downfield shift was also

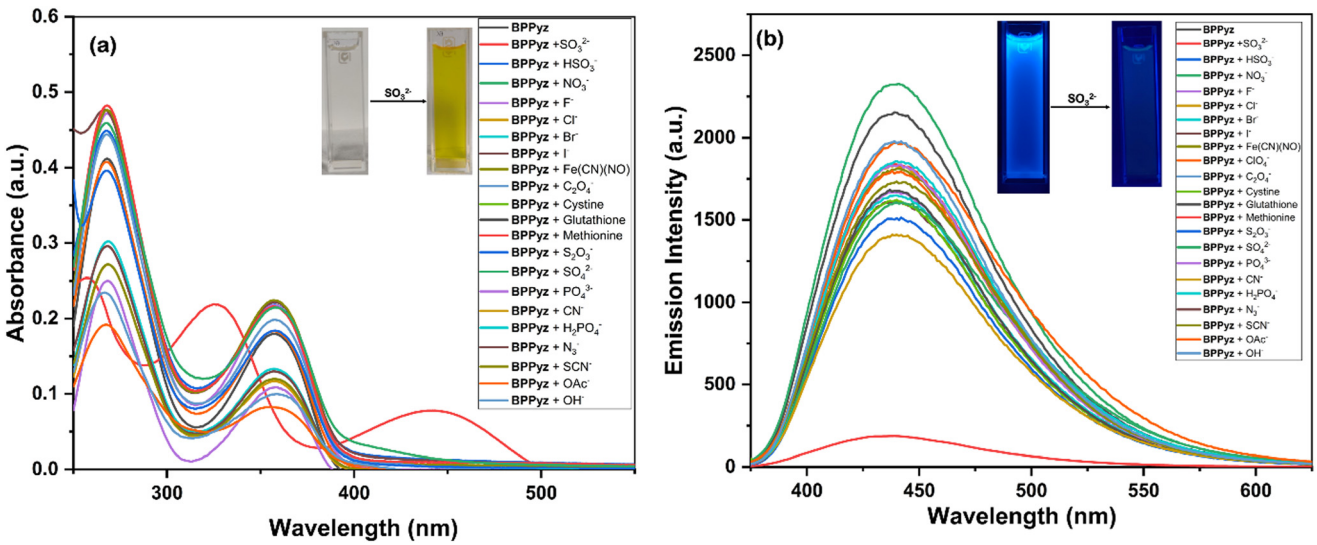

Fig. 7 (a) Absorbance and (b) fluorescence spectra of **BPPyz** (2×10^{-5} M) with different anions.

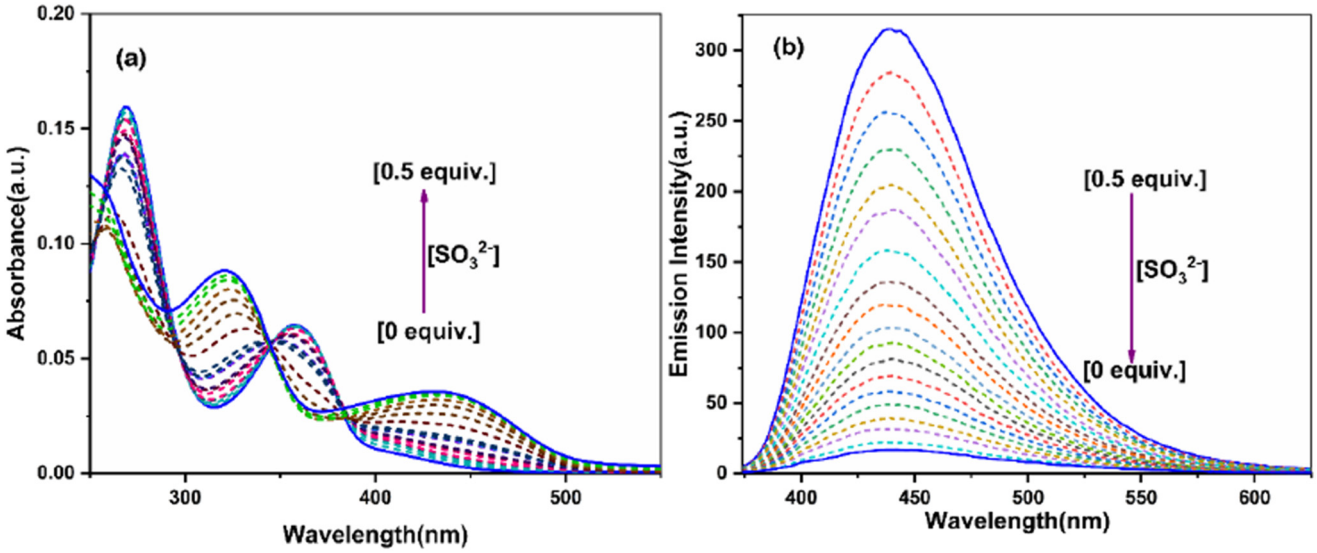

Fig. 8 (a) Absorbance and (b) fluorescence spectra of **BPPyz** (2×10^{-5} M) with different amounts of SO_3^{2-}.

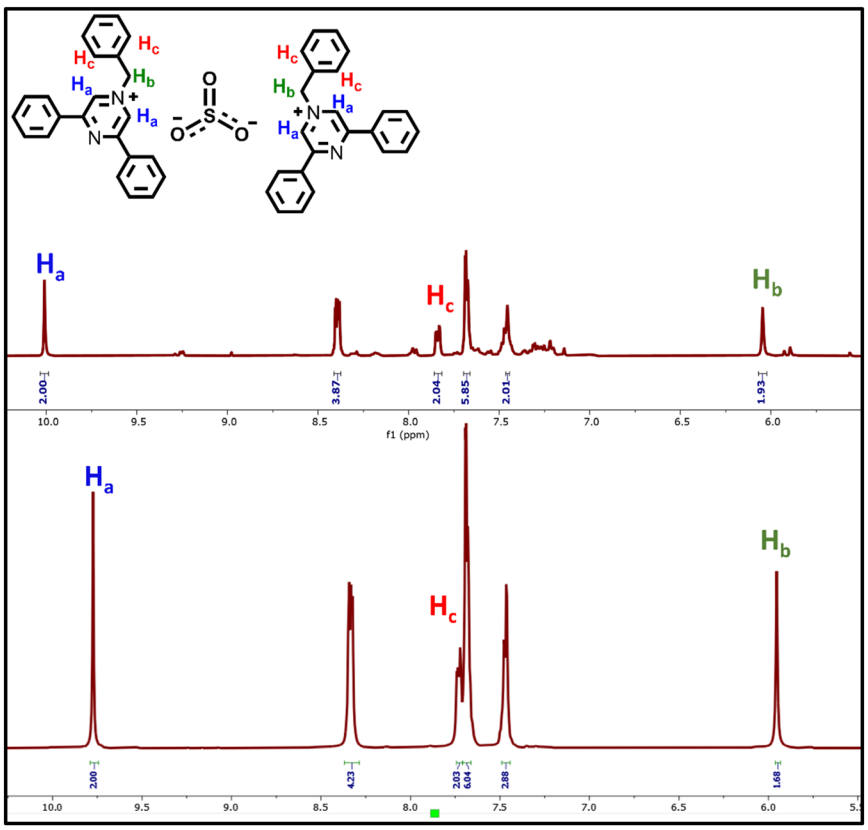

Fig. 9 ^{1}H NMR spectra of the **BPPyz**–SO_3^{2-} complex.

observed in the aliphatic proton (H_b) and aromatic proton (H_c) signals due to hydrogen bonding (Fig. 9).

The DFT calculations were carried out at the B3LYP/6-311G(d,p) level of theory to understand the formation of the complex (Fig. 10a). The red-shifted absorption band in **BPPyz**–SO_3^{2-} can be explained by the molecular orbitals. In the **BPPyz**–SO_3^{2-}complex, the energy gap between the HOMO and the LUMO was −0.519 eV, which is much smaller than that in **BPPyz** (−1.95 eV). Such lowering of the HOMO–LUMO gap in the **BPPyz**–SO_3^{2-} complex can be attributed to the change in the electron distribution due to anion exchange (Fig. 10b).

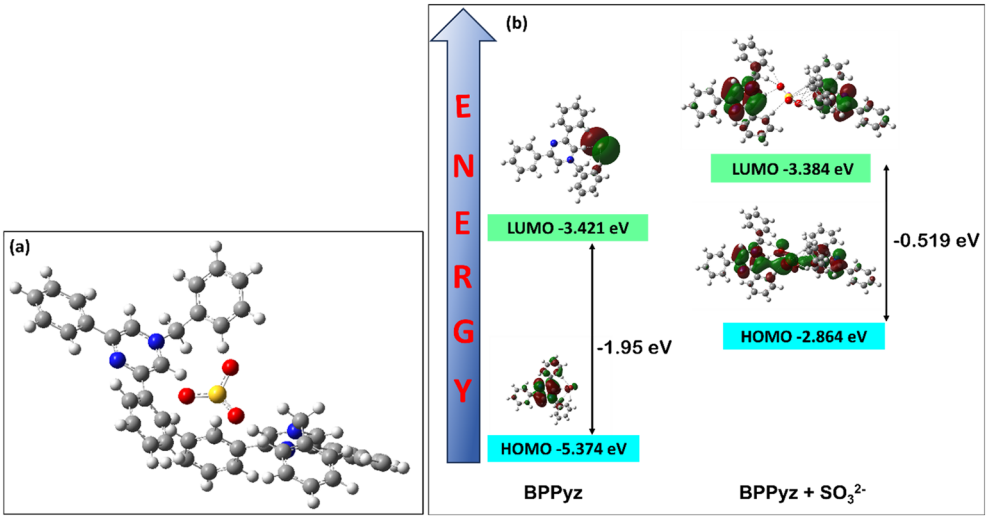

Fig. 10 (a) Optimized ball-and-stick model and (b) frontier molecular orbitals of **BPPyz**–SO_3^{2-}.

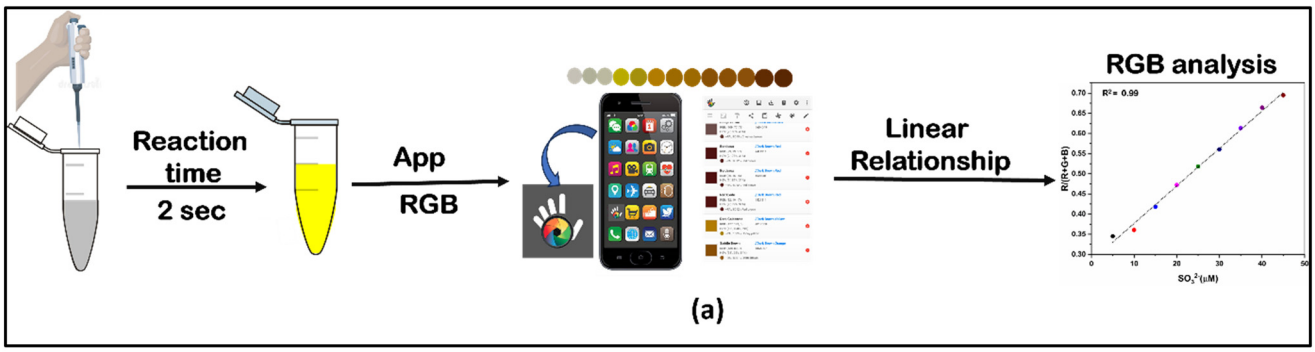

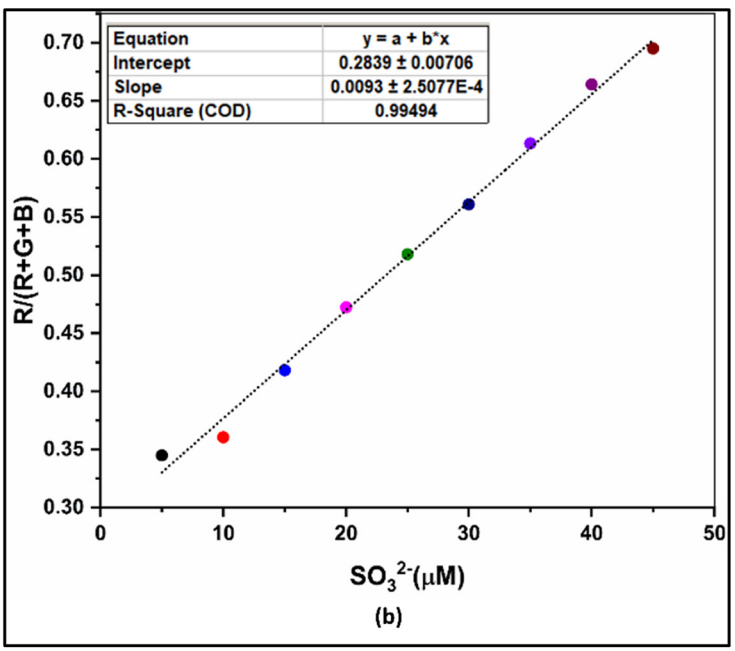

Fig. 11 (a) Integration of the **BPPyz** chemosensor with a smartphone and (b) the ratio of R/(R + G + B) *versus* SO_3^{2-} concentration in the range of 0 to 20.0 μM.

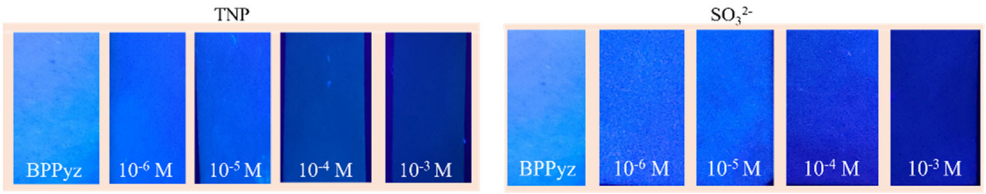

Fig. 12 Test paper strips for the detection of TNP and SO_3^{2-} under 365 nm UV light.

3.4 Smartphone-based colorimetric read-out

An affordable on-site monitoring method was developed based on the naked-eye detectable change of **BPPyz** in the presence of SO_3^{2-} using a smartphone (Fig. S34†). The standard RGB scale is represented by whole number values from 0 to 255 for red, green, and blue colors. The values [0, 0, 0] and [255, 255, 255] correspond to absolute black and white, respectively. The change in the RGB values of **BPPyz** on the addition of SO_3^{2-} was recorded by keeping the smartphone camera about 1 cm away from the vials enclosed inside a paper box. The changes were recorded using a smartphone app, which could directly output the RGB values (Fig. 11a). In order to compute the fitting parameters, several empirical formulae were used to assess the correlation of the RGB values processed from the smartphone (Fig. S35†). The optimal relationship was obtained when the ratio of R/(R + G + B) was used (Fig. 11b). By using this ratio, a calibration curve was obtained with good linearity from 0 μM to 20.0 μM (R^2 = 0.9949). These results demonstrate that the developed smartphone-based colorimetric read-out method performs well and is more accessible, affordable, and portable than other chromatographic techniques.

3.5 Implementation of test paper strips

For rapid and on-site detection of TNP and sulfite, commercial Whatman filter paper was used to create paper test strips.[60] The strips were dipped in a concentrated **BPPyz** solution for 10 minutes, and then allowed to dry for two hours. These test strips were dipped in aqueous solutions of TNP and sulfite solutions (10^{-3}–10^{-6} M), and fluorescence quenching was seen under a 365 nm UV lamp (Fig. 12).

Conclusion

In summary, a pyrazinium-based fluorescent chemosensor, **BPPyz**, was successfully synthesized, and its photophysical properties were studied in detail. In aqueous media, **BPPyz** showed high selectivity and high sensitivity for sensing TNP among nitro compounds by fluorescence quenching, which can be due to the formation of the ground state charge transfer complex and resonance energy transfer. Among anions, **BPPyz** exhibits good sensing ability towards SO_3^{2-} by colorimetric and fluorometric responses attributed to hydrogen bond interactions between the pyrazinium of **BPPyz** and SO_3^{2-}. Moreover, **BPPyz** was integrated with a smartphone for sulfite detection. The developed strategy is portable and accessible for *in situ* sulfite analysis and does not require advanced instruments.

Author contributions

Pragya: conceptualization, methodology, data curation, validation, and writing the original draft. Krishnan Rangan: data curation, writing, and reviewing the draft. Bharti Khungar: conceptualization, supervision, writing, and reviewing and editing.

Conflicts of interest

There are no conflicts of interest to declare.

Acknowledgements

The authors acknowledge financial support from the Science & Engineering Research Board (SPG/2021/004711), DST-FIST [SR/FST/CSI-270/2015], UGC-SAP, and BITS Pilani for instrumentation facilities. Pragya thanks BITS Pilani for the fellowship.

References

1 P. Vadivel, K. Dayanidhi and N. Sheik Eusuff, *Sens. Diagn.*, 2023, **2**, 1311–1321.
2 A. S. Tanwar, N. Meher, L. R. Adil and P. K. Iyer, *Analyst*, 2020, **145**, 4753–4767.
3 Y. Liu, Y. Wang, L. Chen and G. Che, *Dyes Pigm.*, 2022, **203**, 110378.
4 S. Chakravarty, B. Gogoi and N. Sen Sarma, *J. Lumin.*, 2015, **165**, 6–14.
5 S. Kasthuri, P. Gawas, S. Maji, N. Veeraiah and N. Venkatramaiah, *ACS Omega*, 2019, **4**, 6218–6228.
6 D. Prabha, D. Singh, P. Kumar and R. Gupta, *Inorg. Chem.*, 2021, **60**, 17889–17899.
7 G. Singh, V. Saini, G. Lal, A. Saraiya and N. Singh, *Mater. Sci. Eng., B*, 2021, **264**, 114970.
8 V. Bhalla, A. Gupta, M. Kumar, D. S. Rao and S. K. Prasad, *ACS Appl. Mater. Interfaces*, 2013, **5**, 672–679.
9 H. Muniyasamy, C. Chinnadurai, M. Nelson, A. Veeramanoharan, M. Sepperumal and S. Ayyanar, *Ind. Eng. Chem. Res.*, 2021, **60**, 7987–7997.
10 S. K. Nandi, S. Roy Chowdhury, D. Podder, P. K. Ghorai and D. Haldar, *Cryst. Growth Des.*, 2020, **20**, 1884–1890.
11 R. Franco, G. Navarro and E. Martinez-Pinilla, *Antioxidants*, 2019, **8**(11), 542.

12 T. Uchacz, G. Jajko, A. Danel, P. Szlachcic and S. Zapotoczny, *New J. Chem.*, 2019, **43**, 874–883.
13 H. Yin, Y. Wu, X. Peng and F. Song, *Chem. Commun.*, 2020, **56**, 10549–10551.
14 H. Zhang, S. Xue and G. Feng, *Sens. Actuators, B*, 2016, **231**, 752–758.
15 S. Liu, L. Song, Q. Sun, Z. Chen, Y. Ge, W. Zhang and J. Qian, *RSC Adv.*, 2015, **5**, 91863–91868.
16 B. Dawidziuk, J. Nawała, D. Dziedzic, D. Gordon and S. Popiel, *Anal. Methods*, 2018, **10**, 5188–5196.
17 M. Liu, W. Zheng, Y. Yang, G. Shi, Y. Li, S. Zhou, Y. Zhao and Z. Yao, *Microchem. J.*, 2023, **191**, 108889.
18 L. R. Terry, S. Sanders, R. H. Potoff, J. W. Kruel, M. Jain and H. Guo, *Anal. Sci. Adv.*, 2022, **3**, 113–145.
19 A. S. Tanwar, S. Patidar, S. Ahirwar, S. Dehingia and P. K. Iyer, *Analyst*, 2019, **144**, 669–676.
20 A. Kumar and P. S. Chae, *Sens. Actuators, B*, 2017, **240**, 1–9.
21 A. Kumar, A. Pandith and H.-S. Kim, *Sens. Actuators, B*, 2016, **231**, 293–301.
22 G. Sathiyan and P. Sakthivel, *RSC Adv.*, 2016, **6**, 106705–106715.
23 J. F. Xiong, J. X. Li, G. Z. Mo, J. P. Huo, J. Y. Liu, X. Y. Chen and Z. Y. Wang, *J. Org. Chem.*, 2014, **79**, 11619–11630.
24 K. Charan Behera, D. Mallick, B. Narayan Patra and B. Bag, *Spectrochim. Acta, Part A*, 2022, **271**, 120934.
25 K. Maiti, A. K. Mahapatra, A. Gangopadhyay, R. Maji, S. Mondal, S. S. Ali, S. Das, R. Sarkar, P. Datta and D. Mandal, *ACS Omega*, 2017, **2**, 1583–1593.
26 A. Hazra, S. Bej, A. Mondal, N. C. Murmu and P. Banerjee, *ACS Omega*, 2020, **5**, 15949–15961.
27 Q. Ilyas, M. T. Waseem, H. M. Junaid, Z. Ali Khan, F. Munir, A. J. Shaikh and S. A. Shahzad, *Spectrochim. Acta, Part A*, 2022, **272**, 120994.
28 N. Jiang, G. Li, W. Che, D. Zhu, Z. Su and M. R. Bryce, *J. Mater. Chem. C*, 2018, **6**, 11287–11291.
29 S. Halder, P. Ghosh, A. Hazra, P. Banerjee and P. Roy, *New J. Chem.*, 2018, **42**, 8408–8414.
30 S. Chen, Y. L. Yu and J. H. Wang, *Anal. Chim. Acta*, 2018, **999**, 13–26.
31 I. A. Rather and R. Ali, *Org. Biomol. Chem.*, 2021, **19**, 5926–5981.
32 A. M. Pisoschi, A. Pop, I. Gajaila, F. Iordache, R. Dobre, I. Cazimir and A. I. Serban, *Microchem. J.*, 2020, **155**, 104681.
33 A. M. Pisoschi and A. Pop, *Open Chem.*, 2018, **16**, 1248–1256.
34 U. T. Yilmaz and G. Somer, *Anal. Chim. Acta*, 2007, **603**, 30–35.
35 L.-J. Zhang, Z.-Y. Wang, X.-J. Cao, J.-T. Liu and B.-X. Zhao, *Sens. Actuators, B*, 2016, **236**, 741–748.
36 L. Săcărescu, A.-L. Chibac-Scutaru, G. Roman, G. Săcărescu and M. Simionescu, *Environ. Chem. Lett.*, 2022, **21**, 561–596.
37 D. Sirbu, L. Zeng, P. G. Waddell and A. C. Benniston, *Org. Biomol. Chem.*, 2019, **17**, 7360–7368.
38 L. Tan, W. Lin, S. Zhu, L. Yuan and K. Zheng, *Org. Biomol. Chem.*, 2014, **12**, 4637–4643.
39 X. Ma, C. Liu, Q. Shan, G. Wei, D. Wei and Y. Du, *Sens. Actuators, B*, 2013, **188**, 1196–120040.
40 Y. Q. Sun, P. Wang, J. Liu, J. Zhang and W. Guo, *Analyst*, 2012, **137**, 3430–3433.
41 S. Paul, T. Majumdar and A. Mallick, *Dalton Trans.*, 2021, **50**, 1531–1549.
42 T. Wei, F. Wang, Y. Chen, J. Qiang, Z. Zhang, T. Chen and X. Chen, *Dyes Pigm.*, 2018, **159**, 322–330.
43 P. Sowmya, S. Prakash and A. Joseph, *RSC Adv.*, 2023, **13**, 2552–2560.
44 J. Wu, W. Liu, J. Ge, H. Zhang and P. Wang, *Chem. Soc. Rev.*, 2011, **40**, 3483–3495.
45 M. E. Moragues, R. Martinez-Manez and F. Sancenon, *Chem. Soc. Rev.*, 2011, **40**, 2593–2643.
46 Y. Hu, S. Long, H. Fu, Y. She, Z. Xu and J. Yoon, *Chem. Soc. Rev.*, 2021, **50**, 589–618.
47 V. Saini, A. Gupta, K. Rangan and B. Khungar, *Dyes Pigm.*, 2020, **180**, 108447.
48 K. Prabakaran, R. Manivannan and Y. A. Son, *Spectrochim. Acta, Part A*, 2023, **285**, 121874.
49 Pragya, V. Saini, K. Rangan and B. Khungar, *New J. Chem.*, 2022, **46**, 16907–16913.
50 O. V. Dolomanov, L. J. Bourhis, R. J. Gildea, J. A. K. Howard and H. Puschmann, *J. Appl. Crystallogr.*, 2009, **42**, 339–341.
51 G. M. Sheldrick, *Acta Crystallogr., Sect. A: Found. Adv.*, 2015, **71**, 3–8.
52 G. M. Sheldrick, *Acta Crystallogr., Sect. C: Struct. Chem.*, 2015, **71**, 3–8.
53 A. D. Becke, *J. Chem. Phys.*, 1993, **98**, 5648–5652.
54 C. Lee, W. Yang and R. G. Parr, *Phys. Rev. B: Condens. Matter*, 1988, **37**, 785–789.
55 M. J. Frisch, G. W. Trucks, H. B. Schlegel, G. E. Scuseria, M. A. Robb, J. R. Cheeseman, G. Scalmani and V. Barone, *et al.*, *Gaussian 09, Revis. C.01.*, Gaussion, Inc., Wallingford, CT, 2009.
56 N. Tripathi, P. Singh and S. Kumar, *New J. Chem.*, 2017, **41**, 8739–8747.
57 E. Vidal, C. E. Domini, D. C. Whitehead and C. D. Garcia, *Sens. Diagn.*, 2022, **1**, 496–503.
58 A. Virgilio, A. B. S. Silva, A. R. A. Nogueira, J. A. Nóbrega and G. L. Donati, *J. Anal. At. Spectrom.*, 2020, **35**, 1614–1620.
59 A. H. Malik, S. Hussain, A. Kalita and P. K. Iyer, *ACS Appl. Mater. Interfaces*, 2015, **7**, 26968–26976.
60 E. Evans, E. F. Gabriel, W. K. Coltro and C. D. Garcia, *Analyst*, 2014, **139**, 2127–2132.